Flow studies in an in-line Silverson 150/250 high shear mixer using PIV

Espinoza, Cyrus; Simmons, Mark; Alberini, Federico; Mihailova, Olga; Rothman, D.; Kowalski, A.j.

DOI:
10.1016/j.cherd.2018.01.028

Contents lists available at ScienceDirect

Chemical Engineering Research and Design

journal homepage: www.elsevier.com/locate/cherd

Flow studies in an in-line Silverson 150/250 high shear mixer using PIV

C.J.U. Espinoza[a,b], M.J.H. Simmons[a], F. Alberini[a,*], O. Mihailova[b], D. Rothman[c], A.J. Kowalski[b]

[a] School of Chemical Engineering, University of Birmingham, Edgbaston, Birmingham B15 2TT, UK
[b] Unilever R&D, Port Sunlight Laboratory, Bebington, Wirral CH63 3JW, UK
[c] Silverson Machines Ltd., Chesham, Buckinghamshire HP5 1PQ, UK

ARTICLE INFO

Article history:
Received 31 October 2017
Received in revised form 3 January 2018
Accepted 12 January 2018
Available online 1 February 2018

Keywords:
Rotor–stator mixer
High shear mixer
Flow number
PIV
Fluid mechanics
Silverson

ABSTRACT

Angle resolved 2-D PIV measurements were taken of the flow inside an in-line Silverson 150/250 high shear mixer, facilitated by a custom built transparent poly methyl methacrylate mixing head. Water was used as the working fluid in the turbulent regime ($120{,}000 < Re < 420{,}000$) and measurements were taken in a field of view encompassing one quarter of the whole mixing head. The effect of the presence of an additional externally driven flow from a pump, and back pressure using an outlet control valve, were examined. The results show that the dominant flow pattern can either be radial or tangential with the former being driven by the external flow at high flow rates and the latter at increasing rotor speeds. Increasing the back pressure promoted tangential flow. Detailed measurements were made of the influence of these parameters upon the mixer flow pattern and calculation of flow number from 2-D PIV data; the latter are strongly influenced by the geometry of the mixer and pipework.

1. Introduction

High shear mixers (HSM), or 'rotor–stator' mixers (RSM), are widely used in industrial processes such as dispersion, emulsification and liquid–liquid homogenisation because of their capability to impose high levels of shear and energy dissipation rates (three orders of magnitude greater than a mechanically stirred vessel) on a relatively small volume of fluid. They are used in the cosmetics, food, home and personal care and pharmaceutical industries for the manufacture of e.g. mayonnaise, detergents, shampoo and conditioner (Zhang et al., 2012) and can be operated in batch, semi-continuous or continuous (in-line) modes. They are also classified as colloid mills, axial and radial discharge RSMs and toothed devices; and existing manufacturers include Ross, Chemineer, IKA work, Siefer, Rayneri and Silverson (Utomo, 2009).

HSMs have a mixing head which consists of a high speed rotor (moving mixing element with a typical tip speed range of 10–50 m s^{-1}) and a stator (fixed mixing element) which are in close proximity to each other (Atiemo-Obeng and Calabrese, 2004), with a rotor–stator (R–S) gap ranging from 100 to 3000 μm (Karbstein and Schubert, 1995). The operating principle of a HSM involves drawing the fluid axially into the R–S gap; subjecting it to high tangential velocity gradients and turbulence (shear rates ranging from 20,000 to 100,000 s^{-1}); and eventually expelling it radially through the stator holes in the form of jets (Utomo et al., 2009; Zhang et al., 2012). HSMs are manufactured in different sizes and geometries to suit a given application.

Regardless of the ubiquity of these devices, publications detailing aspects of their design and basis of operation have only become available over the last decade. Thus, previous

* Corresponding author.
E-mail addresses: CJE002@bham.ac.uk (C.J.U. Espinoza), F.Alberini@bham.ac.uk (F. Alberini).
https://doi.org/10.1016/j.cherd.2018.01.028

Nomenclature

Symbols

B	rotor blade width, m
D	filled volume diameter, m
D_h	stator hole diameter, m
$D_{ps,inner}$	primary stator inner diameter, m
$D_{ps,outer}$	primary stator outer diameter, m
$D_{r,i}$	inner rotor diameter, m
$D_{r,o}$	outer rotor diameter, m
$D_{ss,inner}$	secondary stator inner diameter, m
$D_{ss,outer}$	secondary stator outer diameter, m
L_{IA}	side length of interrogation area, m
L_p	side length of interrogation area, pixels
$\dot{m}$	mass flow rate, kg h^{-1}
N	rotor speed, rps
N_Q	flow number, dimensionless
P_1	point coordinates (m, m)
P_2	point coordinates (m, m)
$Q_{fit,integrated}$	calculated volumetric flow rate from a fitted function, m^3 s^{-1}
$Q_{measured}$	measured volumetric flow rate using a flow meter, m^3 s^{-1}
Q_{plug}	calculated volumetric flow rate using plug flow approximation, m^3 s^{-1}
Q_{surf}	calculated surface flow rate, m^2 s^{-1}
Q_T	total volumetric flow rate, m^3 s^{-1}
r	arbitrary radial distance in cylindrical coordinates, m
R	filled volume radius, m
r, θ, z	radial, tangential and axial directions in cylindrical coordinates, m
S	magnification, dimensionless
S_r	row separation distance, m
$\bar{U}$	mean velocity, m s^{-1}
U	instantaneous velocity, m s^{-1}
U_{hole}	stator hole velocity, m s^{-1}
U_{max}	maximum velocity, m s^{-1}
U_r	radial component of velocity in cylindrical coordinates, m s^{-1}
U_{rms}	root mean square (RMS) velocity, m s^{-1}
U_{tip}	rotor tip speed, m s^{-1}
U_x	x-component of velocity in Cartesian coordinates, m s^{-1}
U_y	y-component of velocity in Cartesian coordinates, m s^{-1}
U_θ	tangential component of velocity in cylindrical coordinates, m s^{-1}
x, y, z	directions in Cartesian coordinates, m
z	arbitrary axial distance in cylindrical coordinates, m
Z	stator thickness, m

Greek letters

Δt	time delay between image pairs, s
θ	tangential angle, radians
μ	fluid viscosity, Pa s
ρ	fluid density, kg m^{-3}

Dimensionless groups

$Re = \frac{\rho N D_{r,o}^2}{\mu}$	Reynolds number, dimensionless

Abbreviations

PO	pump only
PS	pump and Silverson
SO	Silverson only
VFO	valve fully open
VPC	valve partially closed

selection of operating parameters has relied on operator experience and trial-and-error (Mortensen et al., 2017). Existing studies for both batch and in-line HSMs focus on the development of scaling rules and features of the turbulence within the mixing head. The majority of studies have either been purely experimental, focussing on droplet break-up (Carrillo De Hert and Rodgers, 2017; Hall et al., 2011; James et al., 2017a; Rodgers and Cooke, 2012; Rueger and Calabrese, 2013a,b; Shi et al., 2013), measurement of power consumption (Cooke et al., 2012; James et al., 2017b; Kowalski et al., 2011; Padron, 2001), or flow visualisation studies using techniques such as Laser Doppler Anemometry (LDA) and Particle Image Velocimetry (PIV) (Mortensen et al., 2011, 2017; Utomo et al., 2008) to study the effects of processing parameters such as pump and rotor settings as well as the influence of stator geometries. Some published work on numerical simulations have employed computational fluid dynamics (CFD) (Håkansson and Innings, 2017; Utomo et al., 2009), with the most recent work focussing on validation of CFD simulations via experiments (Jasińska et al., 2013, 2015; Qin et al., 2017; Utomo et al., 2008; Xu et al., 2013; Zhang et al., 2017).

Despite the above efforts, the number of published studies remains low and their generic applicability are limited due to the plethora of factors that needs to be considered to characterise fluid flow behaviour such as: mixer specifications, processing conditions, rotor and stator geometries as well as the mixing mechanisms and applications. Generic scale-up rules do not exist and indeed Mortensen et al. (2011) stated that: "a general characterisation of rotor–stator mixer performance by simple mechanistic models does not seem realistic". The implication is that robust and validated CFD based models are a necessary tool for the practising engineer.

There is an increasing industrial interest in switching from batch to in-line operation of HSMs because of its economic edge in terms of larger throughput and continuous operation (Qin et al., 2017). However, the lack of theoretical knowledge, even more than for batch operated HSMs, makes their design and application even more challenging (Håkansson and Innings, 2017). Some recent studies on pilot-scale in-line HSMs by Xu et al. (2013), Zhang et al. (2017) and Qin et al. (2017) follow the above approach of validating CFD models. They have all collectively evaluated, both numerically and theoretically, parameters such as hydrodynamics (flow pattern) and power consumption in a FLUKO® mixer that are critical in emulsification processes. These parameters allow the characterisation of breakup mechanisms and calculation of energy dissipated in the mixing head.

In this study, angle resolved 2-D PIV measurements are carried out to characterise the flow field inside a custom built, pilot-scale, in-line Silverson 150/250 HSM, using water as the working fluid (single phase flow). The effects of process parameters such as rotor speed, external pump flow rate and back pressure were investigated. The velocity fields are analysed to determine overall flow structures as well as flows near

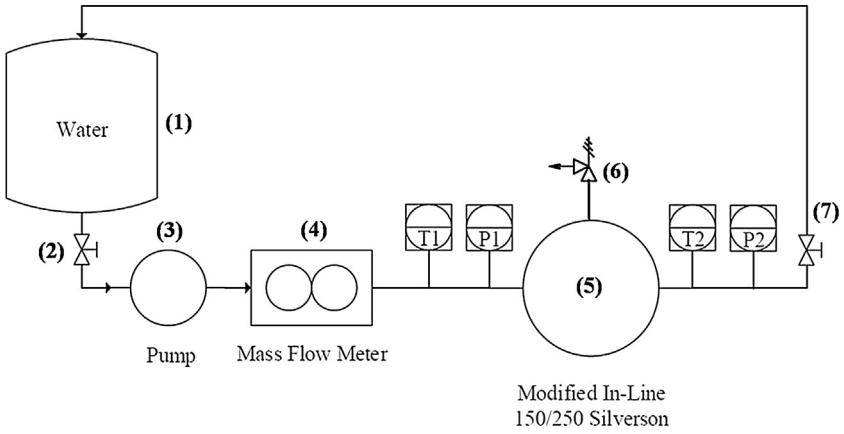

Fig. 1 – Schematic of the experimental arrangement.

the stator holes and mixer flow number. The ultimate aim of this work is to contribute towards guidelines for the design and optimisation of in-line HSMs.

2. Materials and methods

2.1. Equipment

A schematic of the experimental rig is shown in Fig. 1. It consists of a 100 L vessel (1) fitted with a ball valve (2) at the outlet (DN25 PN25, NTC); a positive displacement pump (3) (DW1/007/7, SPX Flow); a Coriolis mass flow meter (4) (Optimass 7000C, Krohne) and a pilot plant scale in-line 150/250 MS Silverson rotor–stator mixer (5) (Silverson Machines Ltd) equipped with pressure (Cerebar M PMP51, Endress+Hauser Ltd) and temperature (PT100, Thermosense) sensors at inlet and outlet and a proportional relief valve (6) (SS-RL4M8F8-SET, Swagelok). A needle valve (7) (SS-16GUF16, Swagelok) controls the back pressure at the mixer outlet. All units are connected with 1″ flexible braided pipes. A vortex breaker is also fitted at the bottom of the vessel (1) to avoid air entrainment.

The geometry of the mixing head is shown in Fig. 2. The front view of the mixing head is shown schematically in Fig. 2a; the mixing head, including the double concentric rotors and double emulsor screens were made out of transparent polymethyl methacrylate for flow visualisation. The internal space within the head has a diameter $D = 108$ mm and the other dimensions of the rotor–stator geometry illustrated in Fig. 2b–d are provided in Table 1. The rotor–stator gap is 0.23 mm and the stator thickness, Z is 15.875 mm.

2.2. Process conditions

Water was used as the working fluid for measurements made in the turbulent regime ($Re > 10{,}000$), where $120{,}000 < Re < 420{,}000$, calculated using

$$Re = \frac{\rho N D_{r,o}^2}{\mu}, \quad (1)$$

where ρ is the density, μ is the viscosity at a fixed temperature, N is the rotor speed and $D_{r,o}$ is the outer rotor diameter.

The pump was used to provide a flowrate, $\dot{m}$ in the mixing head (750–1250 kg h^{-1}) and the rotor speed, was controlled independently (1800–6200 rpm) (30.0–103.3 rps); both were controlled using frequency inverters. The needle valve was also used to control the flow rate and back pressure, with the relief valve set at 5 bar (below the pressure rating of the mixing head of 7 bar). A data recorder (Memograph RSG45, Endress+Hauser) was used to log the mass flow rate, rotor speed, as well as the pressure and temperature at the mixer inlet and outlet. Flow meters were calibrated using the bucket and timer method and were found to be accurate within 1.3% in all experiments.

The parameters used for each experiment are summnarised in Table 2. Runs 1–3 were carried out using the external pump only (PO), whereas runs 4–5 were carried out using the Silverson mixing head only with the pump switched off (SO). Runs 6–8 and 9–11 were carried out with both pump and Silverson operating but with the outlet back pressure valve set either fully open (VFO) or partially closed (VPC) respectively. For VPC conditions, the needle valve was set to achieve the (PO) flowrate prior to switching the Silverson on so that the external pump controls the overall process flow rate. This is done to prevent Silverson acting as a pump.

2.3. PIV experiments

2-D PIV measurements taken were angle resolved to the rotor position as defined in Fig. 2d. The PIV system consists of a dual head 532 nm Nd-Yag laser (Litron Nano PIV) pulsing from 10 to 100 Hz, a 4 megapixel (2048 pixel × 2048 pixel) single frame-straddling 12 bit CCD camera (630091, TSI Inc., USA), a synchroniser (610036, TSI Inc., USA) and a personal computer installed with TSI Insight 4G software. The laser light arm outlet and camera were mounted on a computer controlled traverse which has a precision of 0.2 mm. An optical tachometer attached to the mixer shaft enabled encoding of the rotor angle by sending a signal to the synchroniser at the 0° position. Other angles were then set by inputting the necessary time delay into the Insight 4G software. Silver coated hollow glass 10 μm diameter spheres with a density of 1400 kg m^{-3} (Dantec Inc., DK) were used as seeding particles. They have a short relaxation time and faithfully follow the fluid motion.

500 image pairs were obtained for each experiment from which the average velocity fields were obtained. Fig. 3 shows that both mean, $\bar{U}$, and rms velocity, U_{rms}, values stabilise after 150 image pairs both in high shear (P_1) and bulk regions (P_2) (Fig. 4a), thus a sample of 500 is more than sufficient to ensure the turbulent features of the flow are captured (Gabriele et al., 2009). The images were processed using a recursive Nyquist grid algorithm using interrogation areas (IA) of 32 × 32 and 16 × 16 pixels for the first and second passes respectively. The

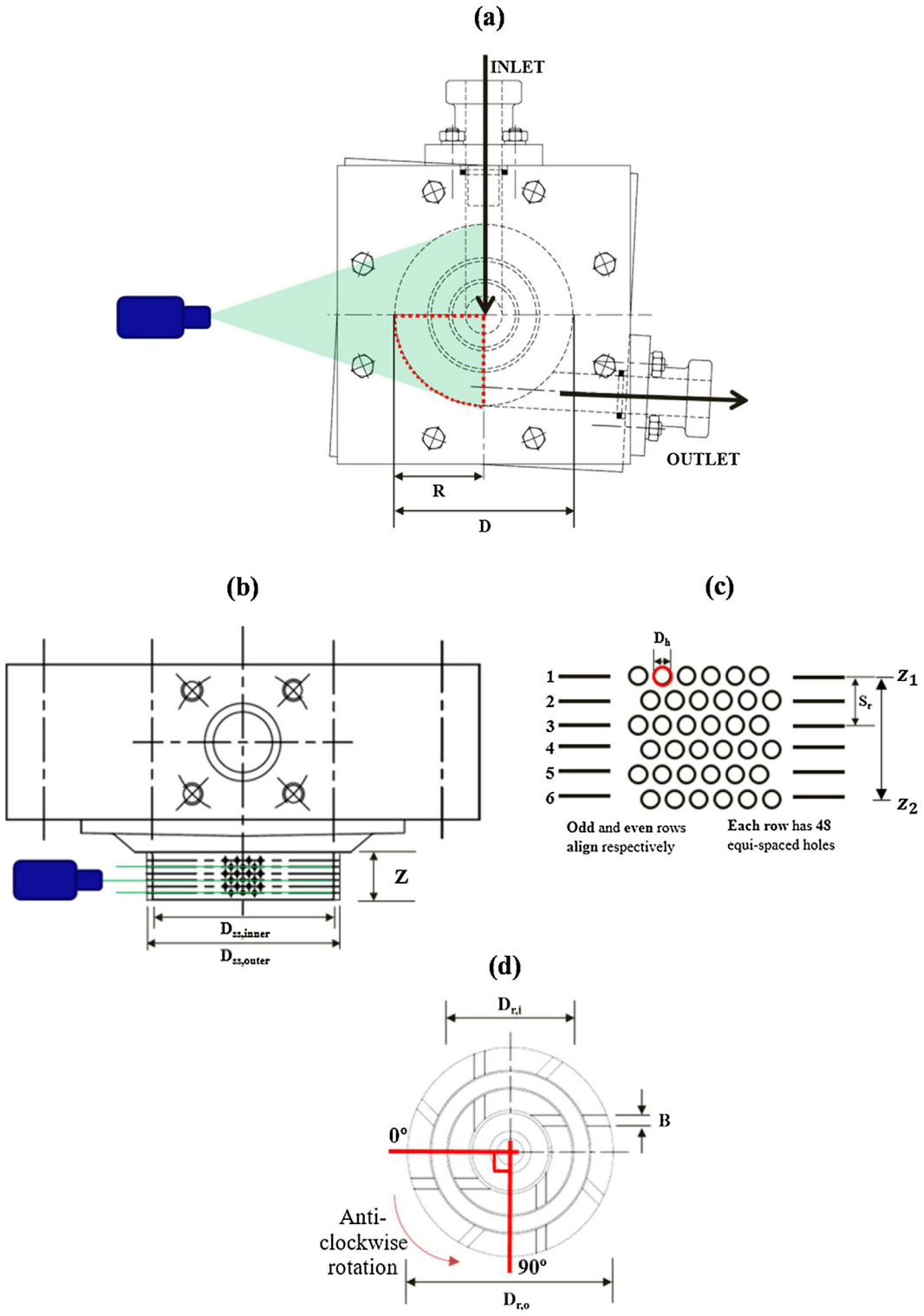

Fig. 2 – (a) Front view of the mixing head showing the inlet, outlet, laser sheet and region of interest, (b) top view of the mixing head showing laser sheet positions, (c) details of the secondary stator and (d) schematic of rotors in 0° position.

Table 1 – Dimensions and details of the rotor–stator.

Item	Inner diameter (mm)	Outer diameter (mm)	Details
Inner rotor, $D_{r,i}$	38.10	–	4 blades Blade width, $B = 3.17$ mm
Outer rotor, $D_{r,o}$	63.50	–	4 blades Blade width, $B = 3.17$ mm
Primary stator (inner screen), D_{ps}	38.56	42.55	- 5 rows of 30 × $D_h = 1.59$ mm circular holes, 150 holes - Separation distance between aligned rows $S_r = 4.75$ mm
Secondary stator (outer screen), D_{ss}	63.96	68.33	- 6 rows of 48 × $D_h = 1.59$ mm circular holes, 288 holes - Separation distance between aligned rows $S_r = 4.75$ mm

Table 2 – Summary of results for different methods of evaluation of flow rates from PIV data.

Run (–)	External pump flow rate, $\dot{m}$ ($kg\,h^{-1}$)	Rotor speed, N (rps)	Flow class (–)	$Q_{measured}$ $\times 10^{-4}$ ($m^3\,s^{-1}$)	Q_{plug} $\times 10^{-4}$ ($m^3\,s^{-1}$)	Q_{plug} error (%)	$Q_{fit,integrated}$ $\times 10^{-4}$ ($m^3\,s^{-1}$)	$Q_{fit,integrated}$ error (%)	Calculated flow number, N_Q (–)
1	750	0	PO	2.08	2.09	+0.38	–	–	-
2	1000	0	PO	2.78	3.04	+9.31	3.34	+20.1	N/A
3	1250	0	PO	3.47	3.90	+12.2	–	–	–
4	0	30.0	SO	0.64	0.50	−21.9	–	–	–
5	0	60.0	SO	1.58	3.13	+98.2	1.59	+0.63	0.0103
6	1000	30.0	VFO	2.95	2.81	−4.92	2.49	−15.6	0.0324
7	1000	60.0	VFO	3.55	4.87	+37.2	3.64	+2.54	0.0237
8	1000	103.3	VFO	5.10	7.68	+50.6	5.15	+0.98	0.0195
9	1000	30.0	VPC	2.78	2.20	−20.7	2.24	−19.4	0.0292
10	1000	60.0	VPC	2.78	3.96	+42.7	2.69	−3.24	0.0175
11	1000	103.3	VPC	2.78	5.88	+112	3.28	+18.0	0.0124

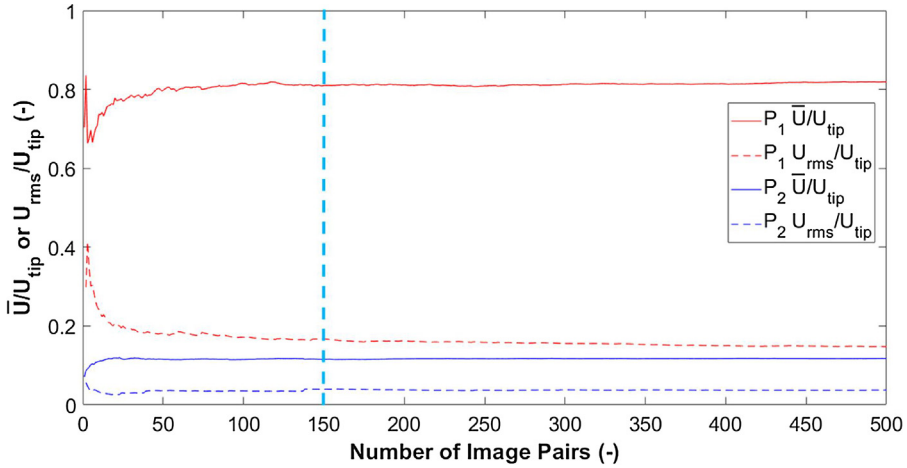

Fig. 3 – Plot of normalised mean velocities ($\bar{U}/U_{tip}$) and root mean square velocities (U_{rms}/U_{tip}) at high shear (P_1) and bulk regions (P_2) indicated in Fig. 4a for the process condition 60.0 rps; 1000 $kg\,h^{-1}$ VFO – row 4 (z = 8.573 mm).

Gaussian peak method by Westerweel (1997) was used to identify individual particles in the image.

The resolution of the PIV measurement depends upon the length scale of the IA, L_{IA}, which acts as a filter below which length scales are not resolved. There is thus a compromise between resolution and field of view. For the experiments performed, the spatial resolution is 38.58 $\mu m\,pixel^{-1}$ which equates to a resolution of 0.62 mm for a 16 × 16 pixel IA, with vectors spaced 0.31 mm apart allowing for 50% overlap of IAs. The time delay between each image in an image pair was calculated in terms of the recommended maximum displacement travelled by a particle within an interrogation area, 0.25 L_{IA} (Adrian, 1986) using

$$\Delta t < \frac{0.25 L_{IA}}{U_{tip}}, \tag{2}$$

where $L_{IA} = S \times L_p$; where S is the magnification factor, L_p is the length of the IA in pixels and rotor tip speed, $U_{tip} = \pi ND$. In post-processing, velocities greater than U_{tip} as well as the vectors that failed the validation stage using the median test (5 × 5 neighbourhood size) were filtered out and replaced with interpolated values from the same grid size.

Despite numerous contributing factors to PIV data uncertainty, PIV system measurements have an accuracy of ~1% to 2% of the full-scale displacement range (Westerweel et al., 2013). The square outer section of the mixing head also ensured that reflections and optical distortion were minimised.

Velocity vectors obtained in Cartesian coordinates are defined as U_x and U_y. Due to the geometry of the filled volume, these values are also converted to cylindrical coordinates as illustrated in Fig. 4, to ease visualisation. The data is first reflected over the line y = −x as shown in Fig. 4a and b (axes relabelled in cylindrical coordinates), which is then transformed into tangential and radial velocity components in the plane of interest (θ, r), defined as U_θ and U_r respectively as portrayed in Fig. 4c. Finally, a section of the field corresponding to the jets emerging from the stator holes is examined in detail, Fig. 4d. Triangular interpolation was also performed using '*gridfit*', a MATLAB® function developed by D'Errico (2005) to evaluate velocity components at a fixed radius across all tangential positions e.g. 3 mm above the outer stator radius, r = 37.2 mm. The result of this process is shown in Fig. 5, where it is demonstrated that the interpolated values track the sparse raw data for r = 37.2 mm ± 0.2 mm. Most of the results, were the ones evaluated for the 4th row of holes in the stator at z = 8.573 mm, Fig. 2c.

Four-fold symmetry is assumed as shown in Fig. 6. It is noteworthy that this assumption is subject to some limitations, for instance, the exit pipe is only present in one quadrant of the mixing head and unfortunately, one that is not suitable for laser access hence its effects on the overall flow pattern were indeterminable.

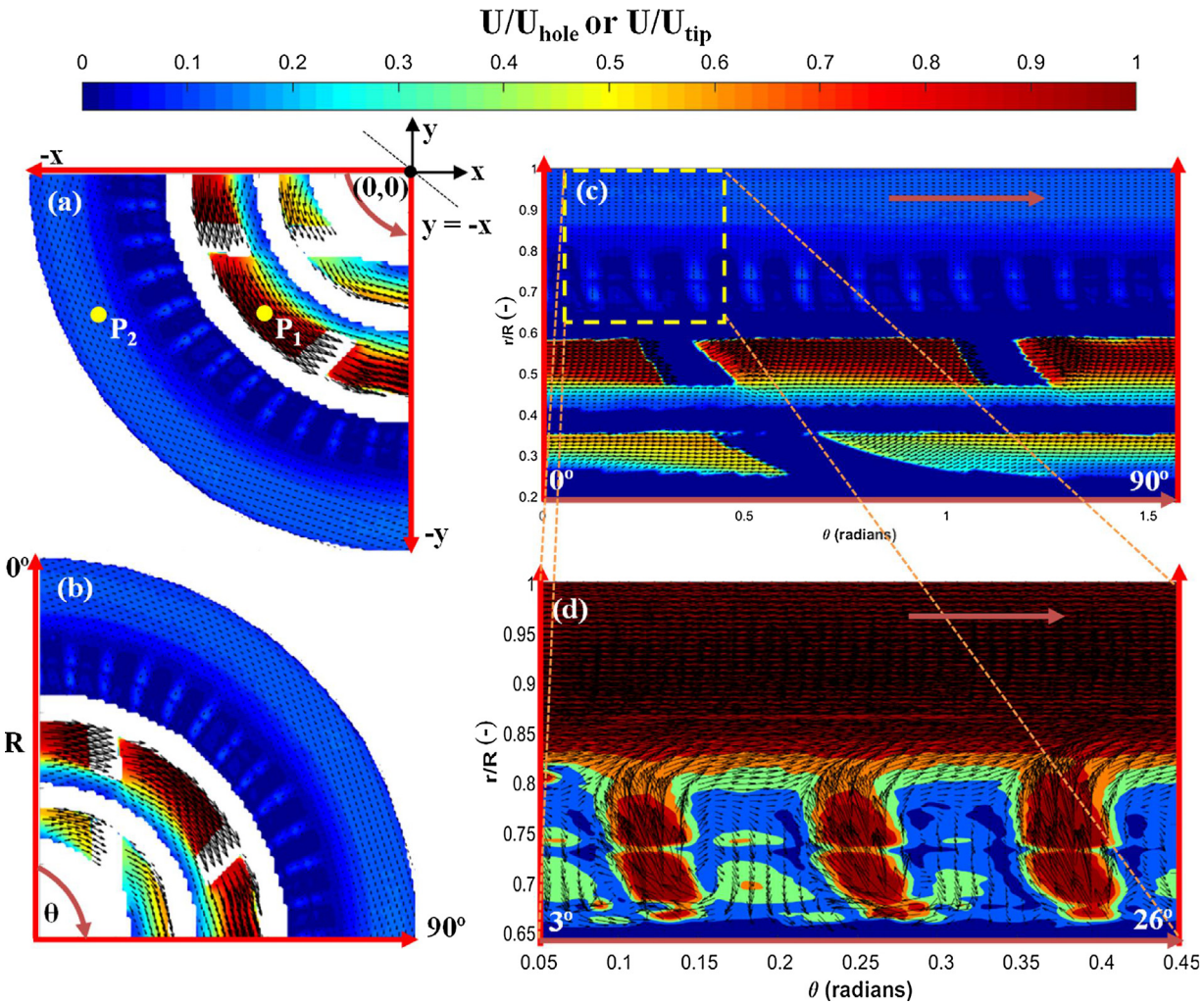

Fig. 4 – Schematic to show how different contour plots were created for the process condition 60.0 rps; 1000 kg h^{-1} VFO – row 4 (z = 8.573 mm) (a) contour plot of raw PIV velocity data in Cartesian coordinates, normalised with U_{tip}, (b) reflection of (a) over the $y = -x$ line (axes re-labelled in cylindrical coordinates), (c) PIV velocity data in cylindrical coordinates, normalised with U_{tip} and (d) zoomed contour plots for better visualisation of jets emerging from the stator holes, normalised with U_{hole}. P_1 and P_2 in (a) are high shear and bulk regions respectively at which average velocities and rms velocities were monitored (Fig. 3).

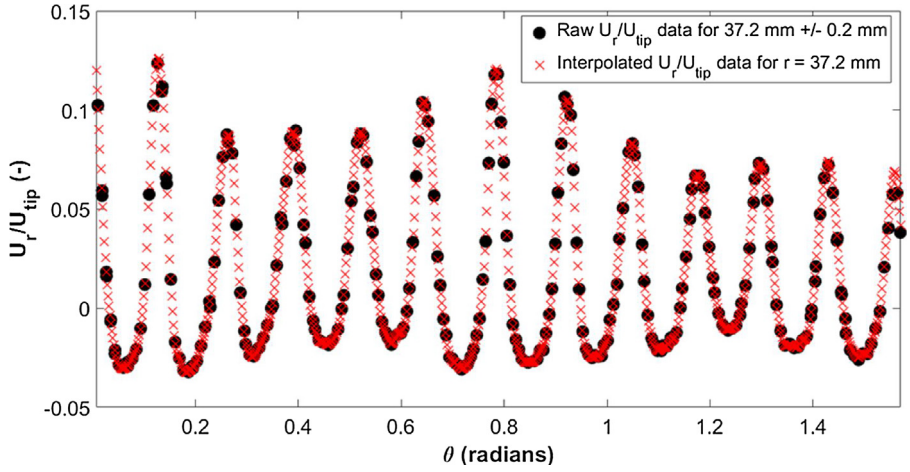

Fig. 5 – Raw data and interpolated values for condition 60.0 rps; 1000 kg h^{-1} PS VFO at r = 37.2 mm – row 4 (z = 8.573 mm).

2.4. *Flow number*

Flow number, N_Q, is a measure of the capability of a mixer to deliver flow, defined as the ratio between the volumetric flow rate, Q_T (m^3 s^{-1}) and a hypothetical flow rate imposed by the rotor:

$$N_Q = \frac{Q_T}{ND_{r,o}^3} \quad (3)$$

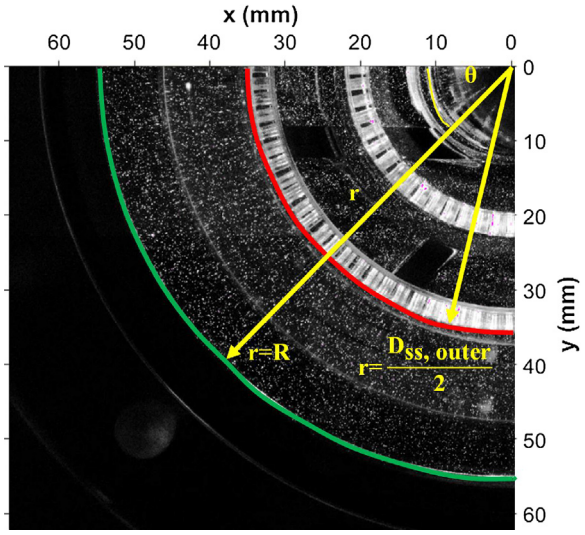

Fig. 6 – Raw image example.

Volumetric flow rate, Q_T is calculated as the net flow through a control surface set normal to the radial flow coming out of the secondary stator. In these experiments this was set as an arc close to the outer secondary stator (red line in Fig. 6) where the radius of the arc could be varied. The minimum distance taken from the outer stator was 1.00 mm to prevent reflections from the rotor which can cause interference in the data. With the symmetry assumption of every 90° or π/2 radians (Fig. 2d), Q_T can thus be calculated from angle resolved PIV measurements using

$$Q_T = 4\int_{z_1}^{z_2}\int_{0}^{\pi/2} rU_r d\theta dz = 4r\sum_{z=z_1}^{z=z_2}\sum_{\theta=0}^{\theta=\pi/2} U_r d\theta dz, \quad (4)$$

where U_r is the radial velocity component, r is the radial distance from the centre of the rotor shaft, z is the axial distance from the middle of the first row of stator holes, z_1 to the middle of the last row of stator holes, z_2 e.g. $z_2 - z_1 = 9.6$ mm (Fig. 2c) and θ is the tangential angle.

Net flow rates were initially calculated using the plug flow approximation. Eq. (4) was simplified to calculate the surface flow rate per unit width ($m^2\,s^{-1}$) from the 2-D data:

$$Q_{surf} = 4r\sum_{\theta=0}^{\theta=\pi/2} U_r d\theta, \quad (5)$$

The resulting value was then multiplied by $6D_h$ (effective stator thickness with fluid flowing out is comprised of the six rows of holes of diameter D_h) to evaluate a plug flow approximation of net flow rate, Q_{plug} ($m^3\,s^{-1}$):

$$Q_{plug} = 6D_h Q_{surf}, \quad (6)$$

The flow number, N_Q of the rotor may also be calculated directly from the relationship between the volumetric flow rate and the set rotor speed e.g. by plotting Q vs N, when the outlet valve is fully open and the external pump is switched off. Since the relationship is linear, the gradient was used to calculate N_Q from Eq. (3). The value obtained, $N_Q = 0.010$, is of similar magnitude to that obtained by Cooke et al. (2012) ($N_Q = 0.050$–0.070) for a similar mixing head. The smaller value obtained in this work is most likely due to differences in the piping system which influence the flow. Moreover, these flow numbers are very small in comparison with impellers used in stirred vessels which are an order of magnitude higher e.g. 0.7 for a Rushton turbine (Hemrajani and Tatterson, 2004). This implies that the rotor has low pumping capability. This is thought to be due to additional flow restrictions in the equipment setup that are not present in conventional stirred vessels e.g. walls of the mixing chamber; presence of flow control elements, pipe fittings and bends; and most importantly the geometry of the double screen stator. The narrow holes within the stator allow for better transfer of tangential momentum from the rotor to the surrounding fluid hence the fluid moves in the tangential direction as opposed to being 'pumped out' in the radial direction (Utomo, 2009).

3. Results and discussion

3.1. *Average flow fields*

Flow patterns of water in the mixing head generated by either the external pump (PO) or Silverson alone (SO) are given in Fig. 7. The corresponding figures for flows with both the pump and Silverson operating (defined as PS) with either VFO or VPC are given in Fig. 8. The velocities shown are either normalised by the calculated hole velocity from the secondary stator, U_{hole} (0.36–0.60 m s^{-1}) or rotor tip speed, U_{tip} (5.98–20.61 m s^{-1}) for ease of illustration. The coordinates (Cartesian: x, y; cylindrical polar: r) are normalised by the inner radius of the mixer head ($D/2 = 54$ mm).

Fig. 7 shows that the normalised velocity fields for both PO and SO conditions are self-similar as would be expected given that the flow is well within the turbulent regime. Moreover, it can also be observed that for PO (Fig. 7a), the flow pattern is dominated by radial discharge jets through the stator holes. This is as expected since there is no mechanism for tangential flow as the rotor is stationary. For SO (Fig. 7b), the flow is dominated by tangential motion due to the motion of the rotor and the highest velocities (0.8–0.9 U_{tip}) are present close to the rotor and in the R–S gap. For PS conditions, a combination of both radial and tangential flows are present as shown in Fig. 8. Due to the possibility of cavitation in the mixer head when the outlet was set at ambient (atmospheric pressure) ($N > 4200$ rpm SO), even with the presence of the external pump, it is necessary to set a back pressure at the outlet to alleviate this. The needle valve installed restricts flow due to its small orifice even when fully open (VFO); the impact of an additional flow restriction through partially closing this valve (VPC), was also investigated.

Fig. 8 shows very subtle differences between VFO and VPC flow fields despite the same pump flow rate (1000 kg h^{-1}) and rotor speed being set ($N = 60.0$ rps). Examining the flows in Cartesian coordinates on the left of the figure, the jet penetration distance is slightly larger for the VFO case than the VPC case, and the velocity magnitudes are slightly larger. It might be expected that partially closing the valve has the effect of increasing the amount of bulk fluid moving tangentially which in effect, decreases the depth of jet penetration.

Detailed analysis of the normalised average radial (U_r) and tangential (U_θ) velocity components are presented in Fig. 9 to quantify the above findings at fixed $r = 37.2$ mm. Fig. 9a confirms the earlier observation that the flow is primarily radial when the flow is delivered by an external pump only (PO), the data for radial velocities are stacked on top of each other and

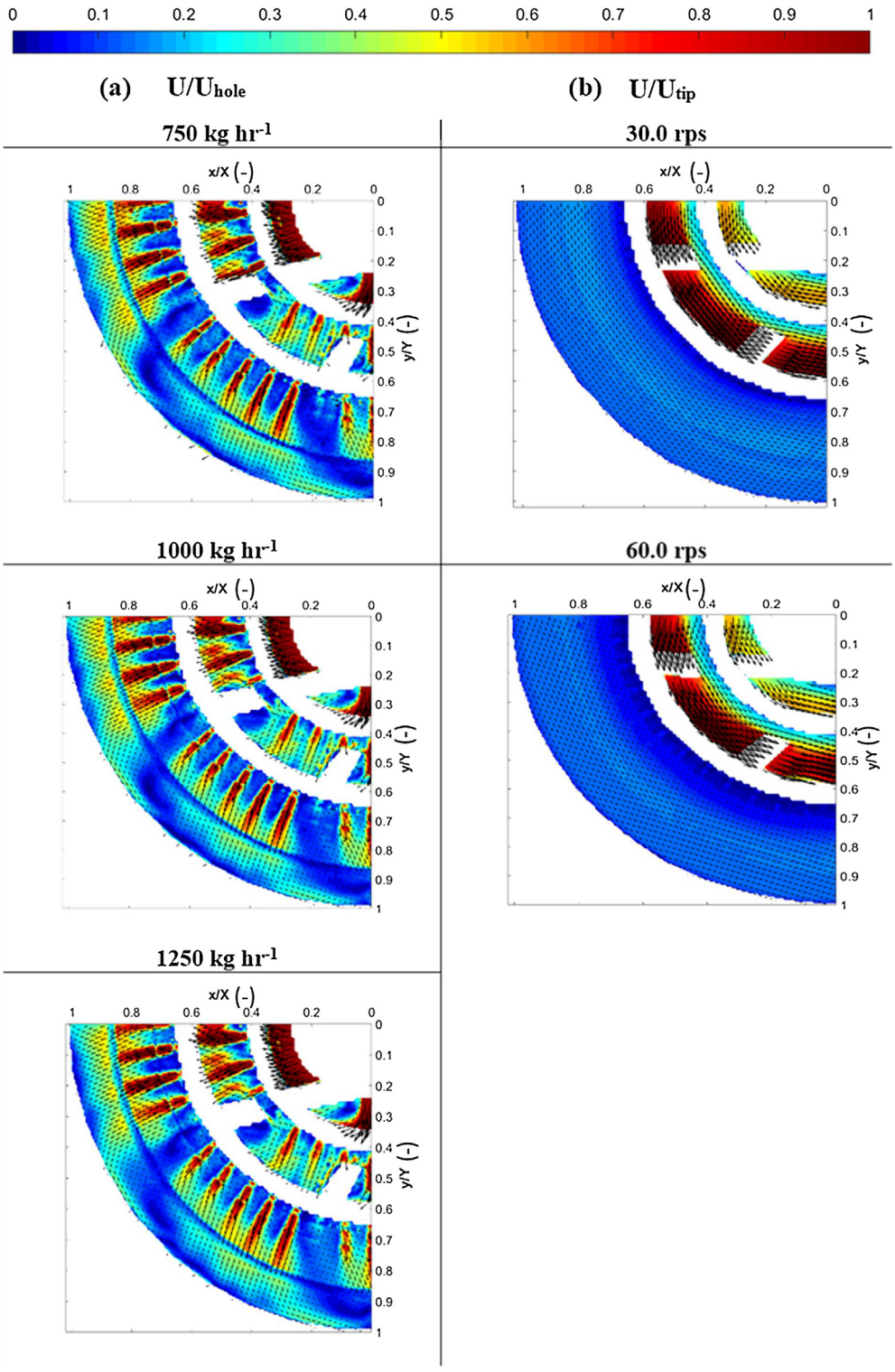

Fig. 7 – Flow patterns generated by (a) pump only (PO) and (b) Mixer/Silverson only (SO) – row 4 (z = 8.573 mm).

the corresponding tangential velocities are practically zero. This is expected as there is no rotational flow generated by the rotor. Conversely in Fig. 9b, when the flow is generated by the Silverson mixer only (SO), both radial and tangential components exist as when the rotor rotates, it pushes the fluid towards the direction of rotation e.g. tangentially anti-clockwise. In addition, due to the stator geometry, jets are also produced when the fluid escapes the volume enclosed by the rotor and the stator. Fig. 9b shows that, at 30.0 rps for SO, the radial and tangential velocities are weakest and strongest respectively, suggesting that the Silverson mixer has poor pumping capability at low rotor speeds and thus the flow is predominantly tangential. As the rotor speed is increased e.g. at 60.0 rps, the balance between radial and tangential components become apparent e.g. the radial velocity increases at the expense of decreased tangential velocity, implying improved pumping capability.

This effect may also be illustrated by examining the effect of introducing a pump flow rate of 1000 kg h^{-1} at 30.0 rps; the governing flow switches from tangential to radial entailing that the external pump has more impact on the overall flow. However, beyond a certain rotor speed e.g. 60.0 rps, there is no

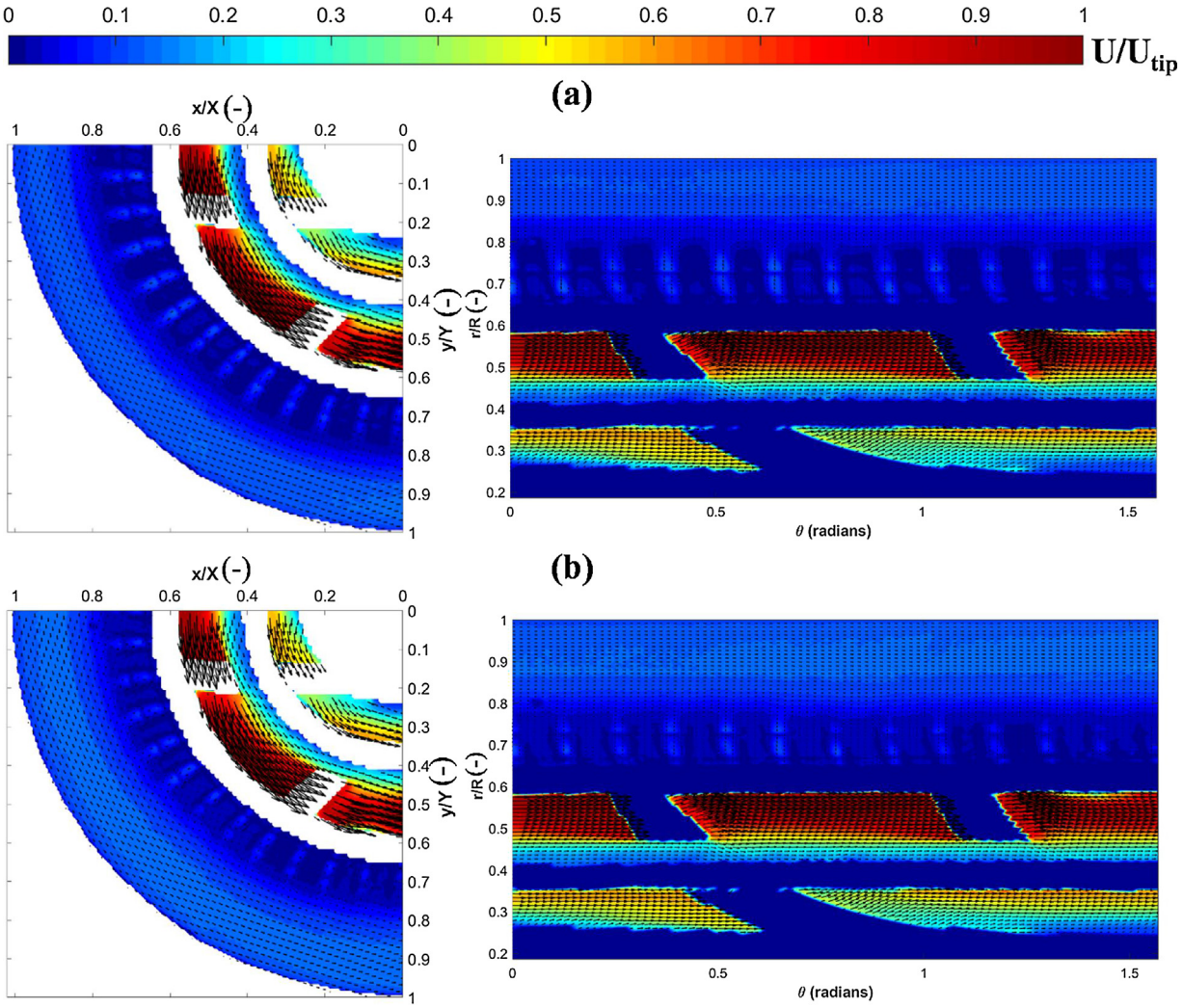

Fig. 8 – Flow patterns generated by both the pump and Silverson mixer (PS) at 60.0 rps; 1000 kg h^{-1} – row 4 (z = 8.573 mm) with (a) valve fully open (VFO) and (b) valve partially closed (VPC). The images on the left and right are in Cartesian and Cylindrical coordinates respectively.

discernible differences in the flow patterns and the tangential flow pattern dominates. This general trend is true for all pump external flow rates examined, but the value of the mixer speed at transition increases with pump flow rate.

In terms of whether the valve is fully open or partially closed (Fig. 9c and d), the radial velocity components are similar whereas, it is evident that the tangential flow significantly increases with rotor speed for VPC conditions (Fig. 9d). This suggests that increasing flow restriction at the outlet results in decreased radial and increased tangential velocities.

3.2. *Effect of radial distance upon the flow fields*

Fig. 10 demonstrates that radial flow velocities dissipate dramatically with increasing radial distance from the outer secondary stator. A region of high radial velocities is found a few mm above the secondary stator ($D_{SS,outer}/2$ = 34.16) e.g. at r = 37.2 mm and lowest near the inner wall of the mixer head e.g. r = 50.2 mm. This is because the stator jets do not penetrate far enough into the bulk fluid. However, the contrary can be observed with tangential velocities; they are strongest near the inner wall because the bulk fluid follows the tangential motion of the rotor, and with increasing radial distance, the bulk flow becomes increasingly free of penetrating jets. Through this, an indication of how far the jet can penetrate the bulk fluid can be obtained e.g. between 44.2 and 50.2 mm.

It was noted above that if the valve is partially closed (VPC), jet penetration distance is decreased and tangential flow is increased as can be observed by comparison of the profiles at r = 44.2 mm between Fig. 10a and b. Another observation is the decreased difference in tangential velocity values between r = 44.2 and 50.2 mm along with their increased magnitudes. These convey that more of the bulk fluid flow tangentially when the valve is partially closed. Since the magnitude of radial velocities are similar when the valve is fully open, it is implied that the energy of the jets is conserved. Thus, this phenomenon can be treated analogous to a short nozzle-to-wall distance configuration for impinging jets.

3.3. *Jet and recirculating flow patterns*

Jets are generated as the fluid flows through the stator holes. Their penetrating distance is greatest when the flow is solely delivered by an external pump as the flow is predominantly radial (Fig. 7a); least when the flow is generated by the Silverson mixer only as the flow is predominantly tangential (Fig. 7b) and governed by selected process conditions in combined flows. Contour plots of average radial and tangential velocities are useful in distinguishing differences between PO

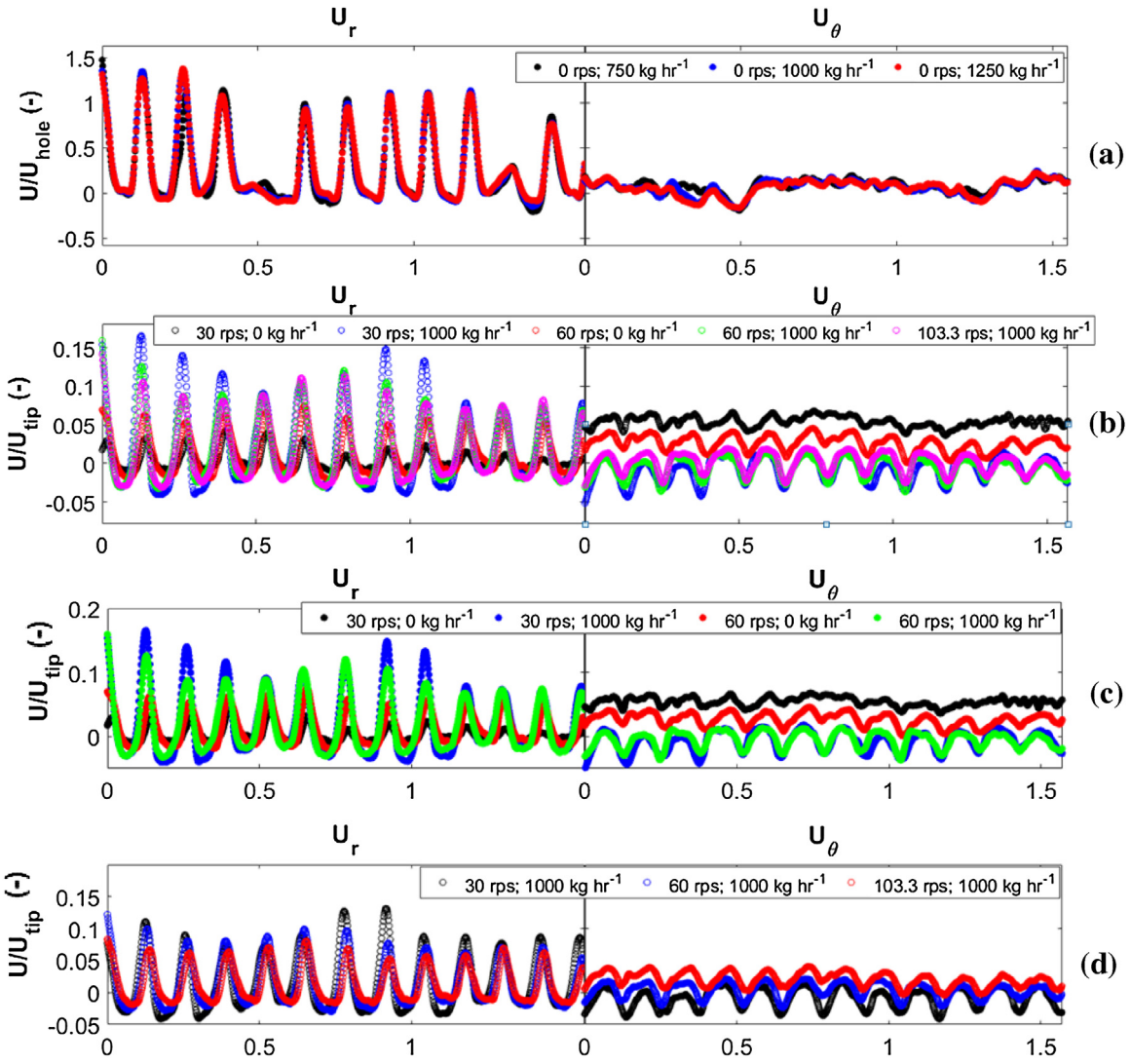

Fig. 9 – Trends of radial and tangential average velocities at varying process conditions at a fixed $r = 37.2$ mm – row 4 ($z = 8.573$ mm) (a) PO only conditions, VFO (b) SO and PS conditions, VFO (c) SO and PS conditions, VFO only (d) PS conditions, VPC only.

and SO conditions because they were normalised with U_{hole} and U_{tip} respectively. However, since PS conditions were also normalised with U_{tip}, the difference between VFO (Fig. 8a) and VPC (Fig. 8b) conditions appeared subtle as jet velocities are much lower in magnitude.

Zoomed contour plots of the jets (between ~3° and 26° or 0.05 and 0.45 radians as demonstrated in Fig. 4) are shown in Fig. 11, normalised with U_{hole} of the combined flow rate (VFO) to emphasise the nature of jet and recirculation flows. From this, it is evident that the length of jet penetration decreases as rotor speed increases (observe the distance of the broken yellow line from the wall in Fig. 11c, e, and g for VFO conditions), which is much more prominent in VPC conditions (Fig. 11d, f, and h). The presence of high velocity jets induce recirculation loops as can be seen from the observed negative radial and tangential velocities e.g. encircled in Fig. 11d. This phenomenon, with the absence of an external pump in the system, was also observed both numerically and experimentally by Utomo et al. (2008, 2009) and Mortensen et al. (2011, 2017) respectively in batch rotor–stator systems. It was found in these studies that regardless of the blade position, jets were centred towards the leading edge of the stator hole while the backflow occurred at the trailing edge. Furthermore, as the jets exit the stator hole, they bend in the opposite direction to the rotor rotation. These are consistent with the results presented in Fig. 11. It is thought that the jets are formed when the leading edge of the rotor blade expels fluid out of the stator hole (momentum flux changes direction from tangential to radial as the fluid hits the surface of the stator's leading edge) while its trailing edge generates a negative pressure that pulls the fluid back in.

Since there are two sources of flow and additional flow control elements e.g. valves are included in the current setup, the flow is very complex. For PO conditions, the jets are comparatively more uniform: straighter and stronger, penetrating closer to the inner wall of the mixer head (Fig. 11a). Recirculation occurs due to jet-to-jet interaction (encircled in Fig. 11a), similar to that observed in multiple impinging jet studies. For SO conditions, hardly any jetting occurs. The reason behind this can be attributed to the stator geometry: Utomo et al. (2009) concluded that for geometries with narrower holes, jets decay within a few millimetres from the holes. This is because these jets are small and have large surface areas, allowing them to efficiently transfer momentum to the surrounding bulk fluid. This also implies that the geometry used has poor

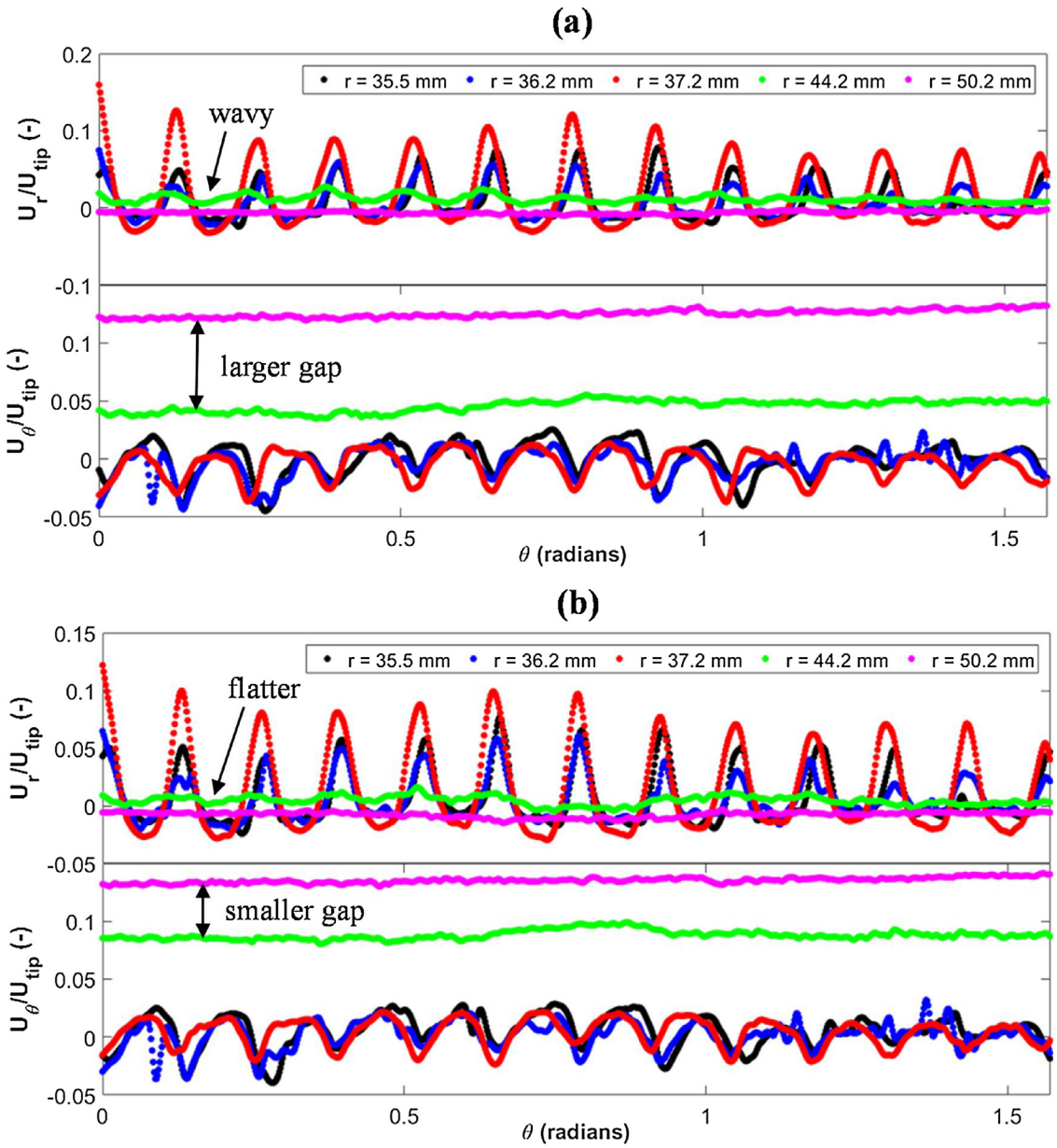

Fig. 10 – Trends of radial and tangential average velocities at varying radii for 60.0 rps; 1000 kg h^{-1}– row 4 (z = 8.573 mm) (a) VFO and (b) VPC.

pumping capabilities and thus the jets are primarily generated by the external pump.

For combined flows (PS conditions), partially closing the outlet valve also has a significant effect on the recirculation loop pattern. At low rotor speeds, the effect is practically negligible as can be seen when comparing Fig. 11c with d. At a higher rotor speed, recirculation is weaker and the fluid tends to accelerate down to the next stator hole (comparing Fig. 11e with f); more of the fluid flows tangentially in the same direction (positive values) as the rotor rotation and jet penetration length is also reduced. These results are shown in 2-D in Fig. 12 for a fixed $r = 37.2$ mm. At an even higher rotor speed (comparing Fig. 11g with h), the overall flow pattern begins to resemble a SO condition. With the valve fully open, the same transition is also observed but occurs at a slower rate; partially closing the valve accelerates this occurrence as portrayed by Fig. 12b where for 103.3 rps VPC, tangential velocities are almost always positive.

3.4. *Flow rate and flow number calculations*

Fig. 13a shows an example of the radial flow components calculated at a fixed $r = 37.2$ mm on row 4 to calculate Q_{surf} while Fig. 13b summarises the results of the flow rates obtained using the plug flow approximation (Eq. (6)) versus the flow rates measured by the flow meter. This plug flow assumption is found to be acceptable when the flow is delivered by the external pump only e.g. values are within confidence intervals of ±20% (in Table 2, errors were calculated as ± % error from the Q_{plug} (or $Q_{fit,integrated}$) = $Q_{measured}$ line). This is because the flow pattern is more uniform in the radial direction as seen in Fig. 11a. Overestimation is expected with this method as the velocity profile is expected to be constrained to zero at the mixer head walls due to the no-slip condition. Since for a fully developed turbulent pipe flow, the maximum centre line velocity, $U_{max} = 1.2\bar{U}$ (Lowe, 1979) and since row 4 can effectively be treated as the centre of the stator, an overestimation of about 20% is expected (hence the confidence interval

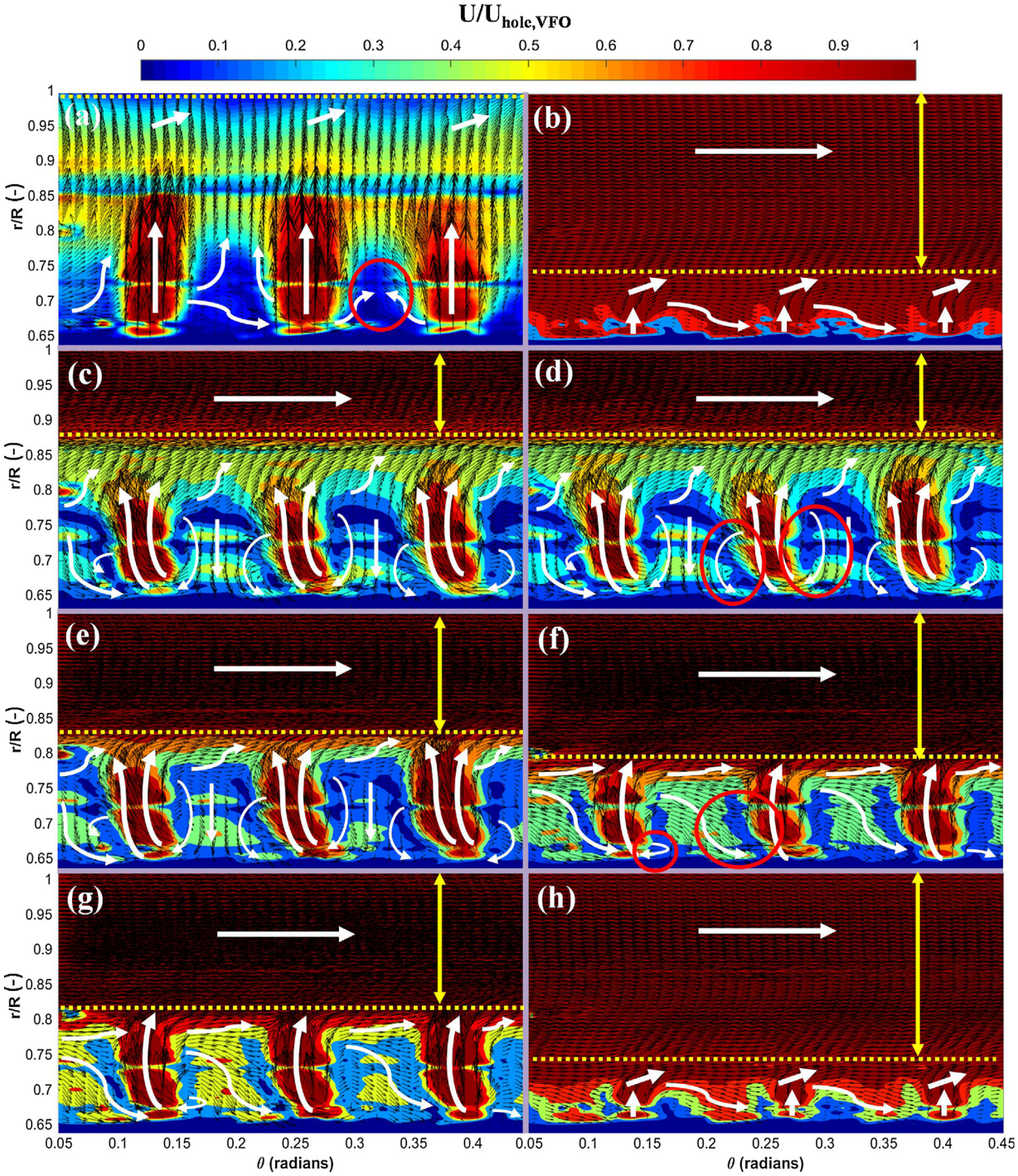

Fig. 11 – Zoomed in velocity fields and contour plots in cylindrical coordinates between 0.05 and 0.45 radians, all normalised with U_{hole} to highlight jet and recirculation flow patterns – row 4 (z = 8.573 mm) for (a) 1000 kg h^{-1} PO, (b) 60.0 rps SO, (c) 30.0 rps; 1000 kg h^{-1} VFO, (d) 30.0 rps; 1000 kg h^{-1} VPC, (e) 60.0 rps; 1000 kg h^{-1} VFO, (f) 60.0 rps; 1000 kg h^{-1} VPC, (g) 103.3 rps; 1000 kg h^{-1} VFO and (h) 103.3 rps; 1000 kg h^{-1} VPC.

of ±20%). Furthermore, significant overestimation is apparent at high rotor speeds but this is due to the increased tangential flow which results in the reduction of fluid recirculation and directing the fluid onto the following jet for both VFO and VPC conditions (Fig. 11). The underprediction for 30.0 rps conditions could be due to the increased recirculation of fluid in comparison with PO conditions as shown in Fig. 11a and c.

More detailed PIV measurements at different z positions enabled Q_{surf} to be calculated from individual stator rows for the same condition e.g. 1000 kg h^{-1} PO; the fitting process is shown in Fig. 14a. The overestimation inherent in a plug flow assumption using the result from row 4 is evident on Fig. 14a.

The results of this improved estimation method for Q_{surf}, are shown in Fig. 14b. The flow numbers calculated using this method are given in Table 2. The value of flow number calculated for 60.0 rps SO is consistent with the calculated N_Q of 0.010. It is not surprising to see that flow numbers increase with additional flow from the external pump at each respective rotor speed as it enhances the pumping capability of the rotor. The values in Table 2 are at a maximum at VFO conditions while the values for VPC conditions are found between SO and VFO conditions. This, again suggests that more of the fluids flow tangentially as the rotor speed begins to control the overall flow pattern inside the mixing head. Moreover, the rate

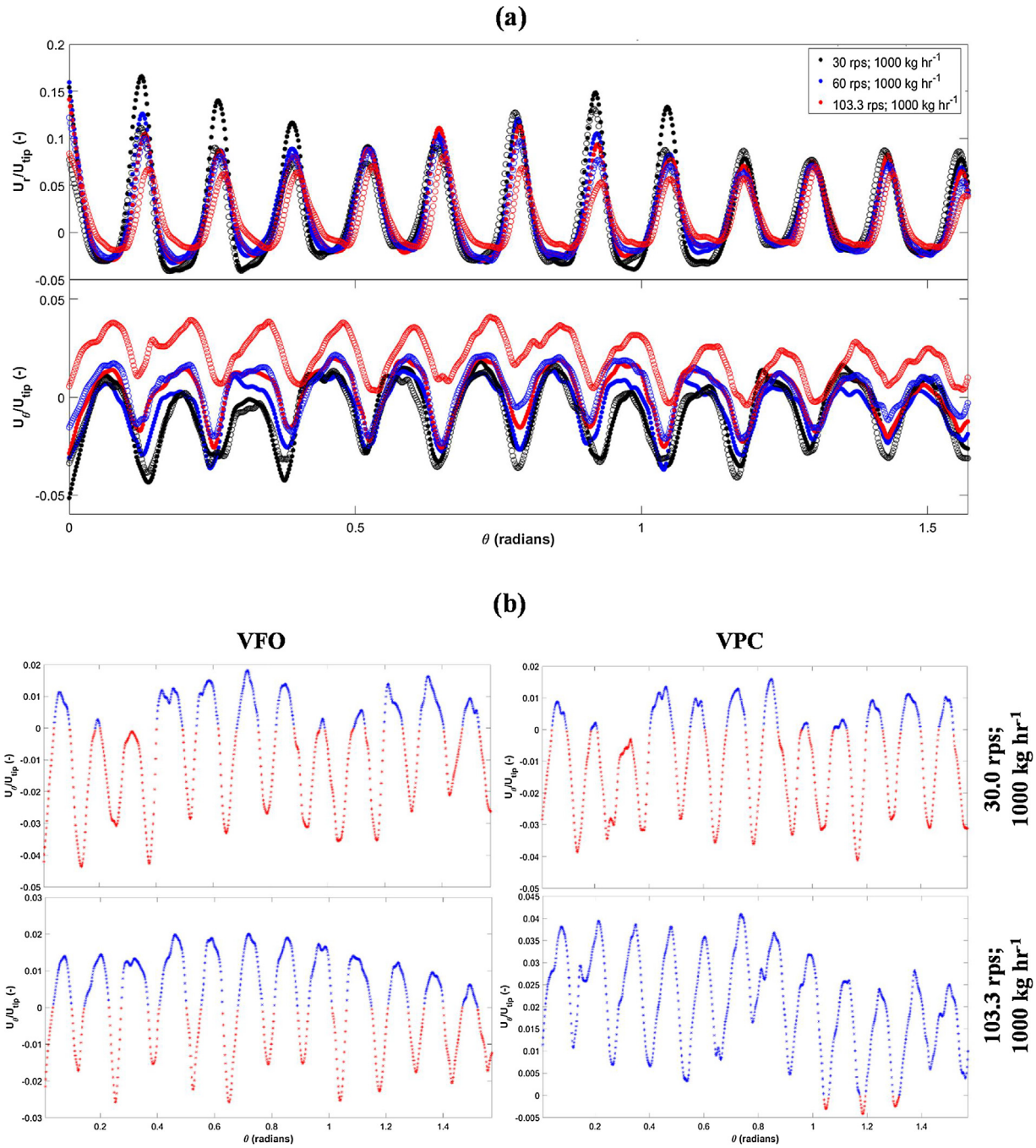

Fig. 12 – VFO vs VPC for 60.0 rps; 1000 kg h^{-1} at fixed r = 37.2 mm – row 4 (z = 8.573 mm) (a) radial (top) and tangential (bottom) velocity trends: filled symbols for VFO, empty symbols for VPC and (b) individual tangential velocity trends where blue and red represent positive and negative velocities respectively. (For interpretation of the references to color in this figure legend, the reader is referred to the web version of this article.)

at which flow numbers decrease back to the original SO values increases with rotor speed.

Overall, although the flow rates for both VFO and VPC conditions are better approximated with this method, since it still does not account for all the effects imposed by the complex flow within the vicinity of the outer stator where interacting multiple jets of fluid are present which is also simulated by Qin et al. (2017), better accuracy is still required to calculate the flow numbers.

3.5. *Implications on emulsification processes for practitioners*

A way to use the information acquired from this study is to explain previously observed trends in recent experimental studies that investigated the effects of process parameters in HSMs upon droplet size distributions. The velocity field data presented can provide a physical insight on the types of dispersion/droplet breakup mechanism that occur in the mixing head. This is important since the flow in Silverson is highly irregular due to different breakup mechanisms that occur simultaneously. For instance, turbulence may not fully develop in the high shear region at short residence times hence simple shear flow may be more important (Hall et al., 2011). In relation to existing experimental results on the same Silverson model obtained by Hall et al. (2011), in terms of:

3.5.1. *Rotor speed at constant flow rate*

Droplet size decreases with increasing rotor speed regardless of dispersed phase viscosity. This suggests that increased tan-

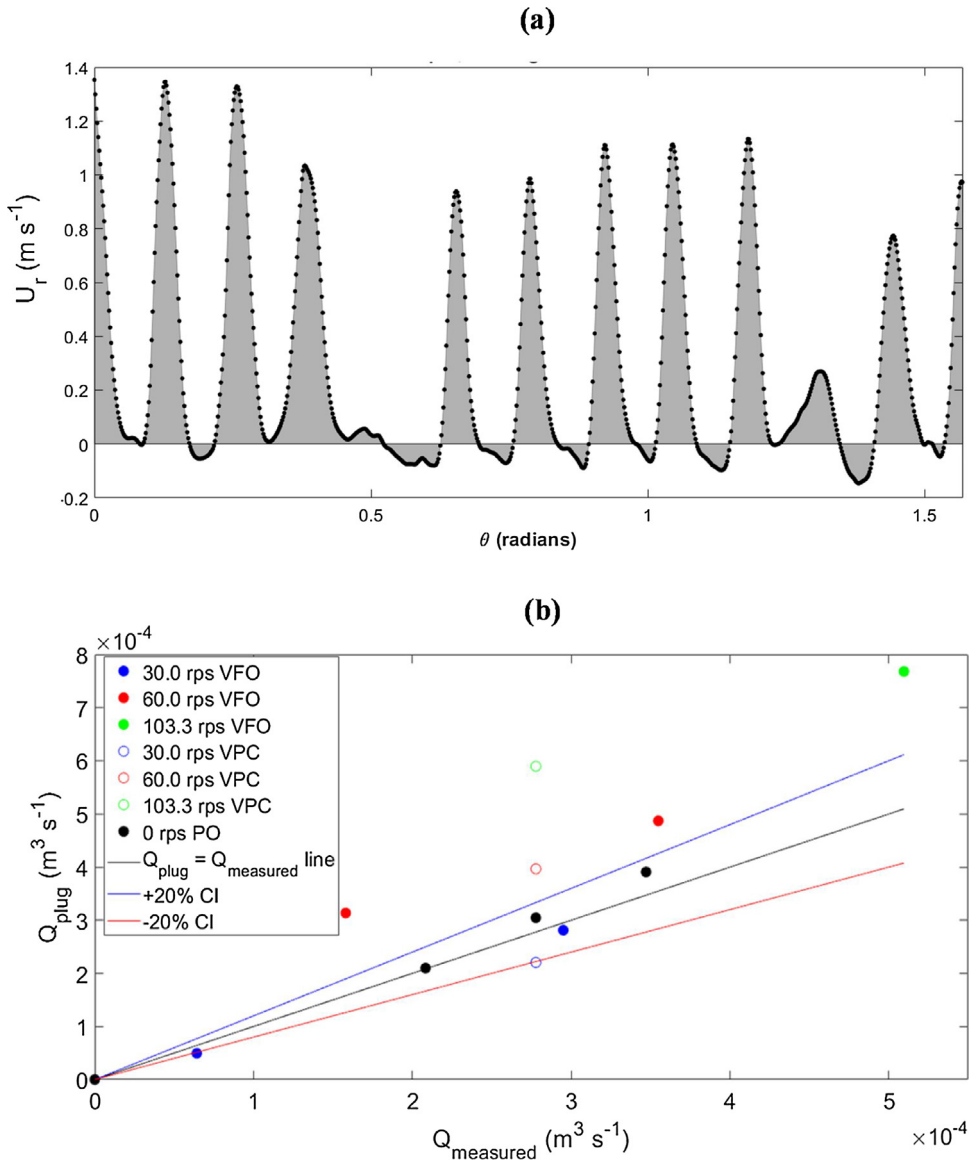

Fig. 13 – Flow rate calculation by plug flow approximation (a) surface area integral for 1000 kg h^{-1} VFO at fixed r = 37.2 mm – row 4 (z = 8.573 mm) and (b) results for varying rotor speeds with 1000 kg h^{-1} external flow rate. (For interpretation of the references to color in this figure legend, the reader is referred to the web version of this article.)

gential flow favours droplet breakup (as found in this study) and implies that the predominant dispersion mechanism is caused by the impingement of fluid on the stator surface (Padron, 2001).

3.5.2. *Flow rate at constant rotor speed*

Hall et al. (2011) also controlled the flowrate using an outlet valve. They found that droplet size was generally independent of flow rate except at relatively high rotor speeds (11,000 rpm) where the droplet size decreased as expected, but seems to have a dependence on flow rate (at lower flow rates) e.g. smaller drops at lower flow rates when the dispersed phase viscosity is low. They attributed this to the effects of breakup mechanisms and residence times. Thus, this highlights the importance of investigating the effects of varying the external pump flow rate for some emulsion systems e.g. longer residence times (at lower flow rates) allow more time for droplet breakup. Thus, the analysis of PIV data can provide both qualitative and quantitative supporting evidence for observed experimental results.

4. Conclusions

There is a need for a standardised way to optimise emulsification processes at the industrial scale. In this paper, a contributing step towards this was done by performing angle-resolved PIV measurements on a 150/250 in-line Silverson high shear mixer. Particular attention was given to the overall flow pattern across the whole mixing head as opposed to existing studies that focus on flow within the stator hole as well as on the effects of varying the external pump flow rate to the overall flow pattern. The goal is to identify how different parameters affect these flow patterns and ascertain how they influence droplet break-up and thus the emulsion quality. With the current equipment setup, the overall flow is comprised of both radial and tangential flows. The former is primarily provided by the external pump while the latter is induced by the rotor. The dominating flow depends on the combination of external pump flow rate and rotor speed. In general, the higher the rotor speed, the more tangential the flow becomes and vice versa. Furthermore, the addition of an outlet valve was also found to promote a more tangential flow.

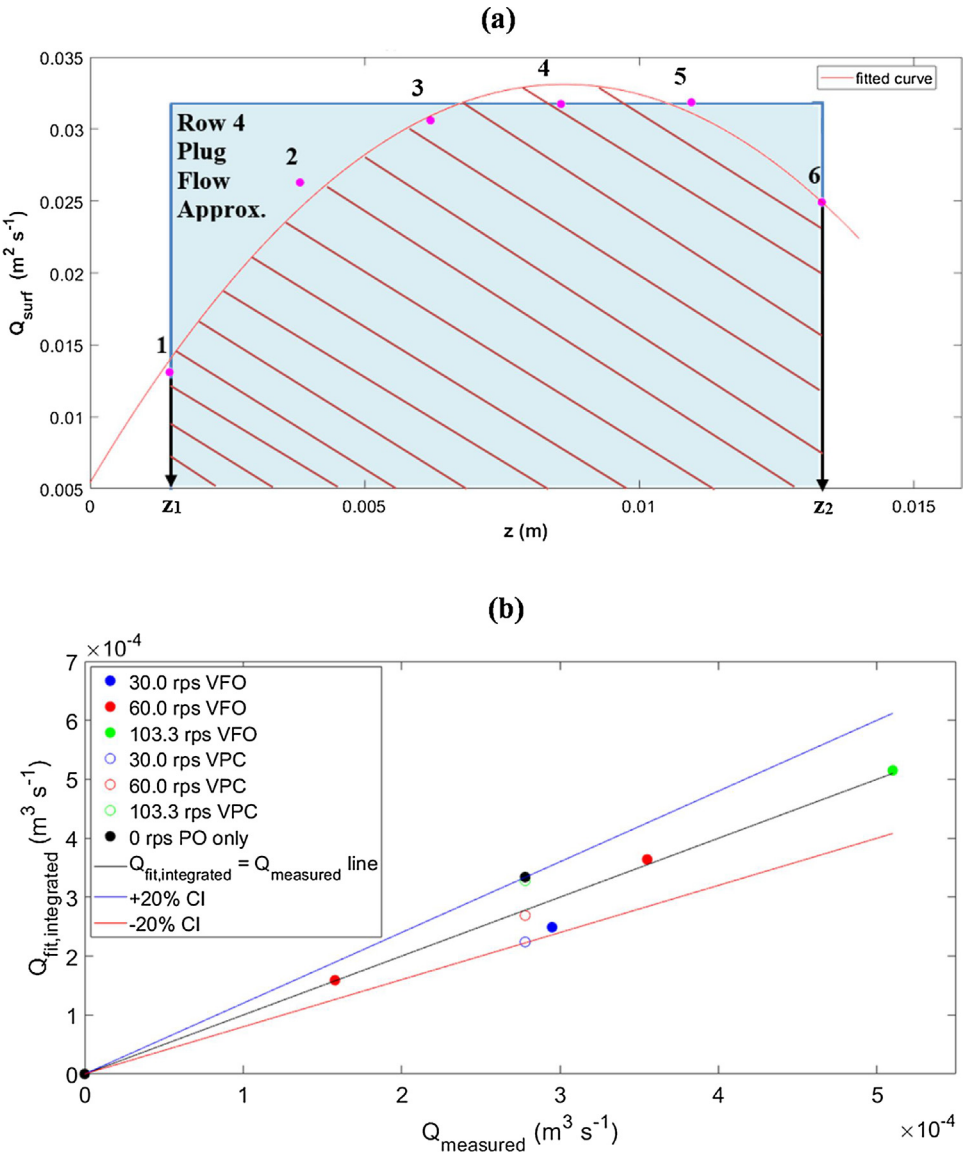

Fig. 14 – Flow rate calculation by evaluating Q_{surf} at all rows at fixed $r = 37.2$ mm (a) integration of fitted curve for 1000 kg h^{-1} VFO across all rows (red hashed area), plug flow approximation for row 4 shown for comparison (shaded light blue area) and (b) results for varying rotor speeds with 1000 kg h^{-1} external flow rate across all rows. (For interpretation of the references to color in this figure legend, the reader is referred to the web version of this article.)

Highest radial velocities were found in close proximity to the outer stator hole (where the jets are) while the highest tangential velocities were present in areas swept by the rotor blades as well as near the wall of the filled volume. Flow rates were evaluated using (a) plug flow approximation and (b) calculating surface flow rates across all rows and fitting a function that is integrated over the effective stator thickness. The former sufficiently predicted flow rates generated by the external pump only while the latter yielded results with better accuracy and was used to calculate flow numbers which are of similar magnitude to those found in literature for a similar mixing head. It was found that the additional flowrate from the pump increased the flow numbers calculated for SO conditions, suggesting that it boosts the pumping action of the rotor. As the rotor speed and extent of flow restriction increase, this additional pumping is diminished and can be linked to the geometry of the outer stator. Narrower holes allow better transfer of the tangential momentum from the rotor to the surrounding fluid hence there is less pumping action as the fluid moves in the tangential as opposed to the radial direction.

Finally, based on the experimental study by Hall et al. (2011), analysis of such results can be attributed to their implication on emulsification processes: a more tangential flow may be attributed to generating smaller droplet sizes due to the dominating breakup mechanism caused by fluid impingement on the stator and the role of the stator becomes more important at higher flow rates.

Acknowledgements

CJUE was funded by the EPSRC Centre for Doctoral Training in Formulation Engineering (EP/L015153/1) and Unilever Research and Development Port Sunlight (UK). The custom-built in-line 150/250 mixing head was supplied by Silverson Machines Ltd.

References

Adrian, R.J., 1986. Image shifting technique to resolve directional ambiguity in double-pulsed velocity. Appl. Opt. 25 (21), 3855–3858.

Atiemo-Obeng, V.A., Calabrese, R.V., 2004. Rotor–stator mixing devices. In: Paul, E.L., Atiemo-Obeng, V.A., Kresta, S.M. (Eds.), Handbook of Industrial Mixing. John Wiley & Sons, Inc., pp. 479–505.

Carrillo De Hert, S., Rodgers, T.L., 2017. Continuous, recycle and batch emulsification kinetics using a high-shear mixer. Chem. Eng. Sci. 167, 265–277.

Cooke, M., Rodgers, T.L., Kowalski, A.J., 2012. Power consumption characteristics of an in-line silverson high shear mixer. AIChE J. 58 (6), 1683–1692.

D'Errico, J., 2005. Surface Fitting Using Gridfit, https://uk.mathworks.com/matlabcentral/fileexchange/8998-surface-fitting-using-gridfit MATLAB Central File Exchange (accessed 29.10.17).

Gabriele, A., Nienow, A.W., Simmons, M.J.H., 2009. Use of angle resolved PIV to estimate local specific energy dissipation rates for up- and down-pumping pitched blade agitators in a stirred tank. Chem. Eng. Sci. 64, 126–143.

Håkansson, A., Innings, F., 2017. The dissipation rate of turbulent kinetic energy and its relation to pumping power in inline rotor–stator mixers. Chem. Eng. Process. 115, 46–55.

Hall, S., Cooke, M., El-Hamouz, A., et al., 2011. Droplet break-up by in-line Silverson rotor–stator mixer. Chem. Eng. Sci. 66, 2068–2079.

Hemrajani, R.R., Tatterson, G.B., 2004. Mechanically stirred vessels. In: Paul, E.L., Atiemo-Obeng, V.A., Kresta, S.M. (Eds.), Handbook of Industrial Mixing. John Wiley & Sons, Inc., pp. 345–390.

James, J., Cooke, M., Kowalski, A., et al., 2017a. Scale-up of batch rotor–stator mixers. Part 2: Mixing and emulsification. Chem. Eng. Res. Des. 124, 321–329.

James, J., Cooke, M., Trinh, L., et al., 2017b. Scale-up of batch rotor–stator mixers. Part 1: Power constants. Chem. Eng. Res. Des. 124, 313–320.

Jasińska, M., Bałdyga, J., Cooke, M., et al., 2013. Application of test reactions to study micromixing in the rotor–stator mixer (test reactions for rotor–stator mixer). Appl. Therm. Eng. 57, 172–179.

Jasińska, M., Bałdyga, J., Cooke, M., et al., 2015. Specific features of power characteristics of in-line rotor–stator mixers. Chem. Eng. Process. 91, 43–56.

Karbstein, H., Schubert, H., 1995. Developments in the continuous mechanical production of oil-in-water macro-emulsions. Chem. Eng. Process. Process Intensif. 34 (3), 205–211.

Kowalski, A.J., Cooke, M., Hall, S., 2011. Expression for turbulent power draw of an in-line Silverson high shear mixer. Chem. Eng. Sci. 66 (3), 241–249.

Lowe, H.C., 1979. Flow in ducts. In: Fluid Mechanics: Theory, Worked Examples and Problems. Macmillan Education UK, London, pp. 156–188.

Mortensen, H.H., Calabrese, R.V., Innings, F., et al., 2011. Characteristics of batch rotor–stator mixer performance elucidated by shaft torque and angle resolved PIV measurements. Can. J. Chem. Eng. 89 (5), 1076–1095.

Mortensen, H.H., Innings, F., Håkansson, A., 2017. The effect of stator design on flowrate and velocity fields in a rotor–stator mixer – an experimental investigation. Chem. Eng. Res. Des. 121, 245–254.

Padron, G.A., MSc Thesis 2001. Measurement and Comparison of Power Draw in Batch Rotor–Stator Mixers. University of Maryland, College Park, MD, USA.

Qin, H., Xu, Q., Li, W., et al., 2017. Effect of stator geometry on the emulsification and extraction in the inline single-row blade-screen high shear mixer. Ind. Eng. Chem. Res. 56 (33), 9376–9388.

Rodgers, T.L., Cooke, M., 2012. Rotor–stator devices: the role of shear and the stator. Chem. Eng. Res. Des. 90, 323–327.

Rueger, P.E., Calabrese, R.V., 2013a. Dispersion of water into oil in a rotor–stator mixer. Part 1: Drop breakup in dilute systems. Chem. Eng. Res. Des. 91, 2122–2133.

Rueger, P.E., Calabrese, R.V., 2013b. Dispersion of water into oil in a rotor–stator mixer. Part 2: Effect of phase fraction. Chem. Eng. Res. Des. 91, 2134–2141.

Shi, J., Xu, S., Qin, H., et al., 2013. Single-pass emulsification processes in two different inline high shear mixers. Ind. Eng. Chem. Res. 52 (40), 14463–14471.

Utomo, A.T., PhD Thesis 2009. Flow Patterns and Energy Dissipation Rates in Batch Rotor–Stator Mixers. The University of Birmingham.

Utomo, A.T., Baker, M., Pacek, A.W., 2008. Flow pattern, periodicity and energy dissipation in a batch rotor–stator mixer. Chem. Eng. Res. Des. 86, 1397–1409.

Utomo, A.T., Baker, M., Pacek, A.W., 2009. The effect of stator geometry on the flow pattern and energy dissipation rate in a rotor–stator mixer. Chem. Eng. Res. Des. 87, 533–542.

Westerweel, J., 1997. Fundamentals of digital particle image velocimetry. Meas. Sci. Technol. 8 (12), 1379.

Westerweel, J., Elsinga, G.E., Adrian, R.J., 2013. Particle image velocimetry for complex and turbulent flows. Annu. Rev. Fluid Mech. 45 (1), 409–436.

Xu, S., Cheng, Q., Li, W., et al., 2013. LDA measurements and CFD simulations of an in-line high shear mixer with ultrafine teeth. AIChE J. 60 (3), 1143–1155.

Zhang, C., Gu, J., Qin, H., et al., 2017. CFD analysis of flow pattern and power consumption for viscous fluids in in-line high shear mixers. Chem. Eng. Res. Des. 117, 190–204.

Zhang, J., Xu, S., Li, W., 2012. High shear mixers: a review of typical applications and studies on power draw, flow pattern, energy dissipation and transfer properties. Chem. Eng. Process. 57–58, 25–41.